Unraveling Precise Locations of Indium Atoms in g-C_3N_4 for Ameliorating Hydrogen Peroxide Piezo-Photogeneration

Hoai Thanh Vuong

hoai-thanh@ucsb.edu

University of California-Santa Barbara https://orcid.org/0000-0001-9669-7209

Nguyen Hoai Anh

Ho Chi Minh City University of Technology - Vietnam National University

Duc-Viet Nguyen

University of Ulsan

Anh Tuyen Luu

Center for Nuclear Technology, Vietnam Atomic Energy Institute

Pham Duc Minh Phan

Ho Chi Minh City University of Technology - Vietnam National University

Huynh Phuoc Toan

Ho Chi Minh City University of Technology - Vietnam National University

Pho Phuong Ly

Ho Chi Minh City University of Technology - Vietnam National University

Quang Hung Nguyen

Duy Tan University https://orcid.org/0000-0002-9739-301X

Ngoc Linh Nguyen

Phenikaa University

Seung Hyun Hur

Pham Thi Hue

Center for Nuclear Technologies

Nguyen Thi Ngoc Hue

Center for Nuclear Technologies

Minh-Thuan Pham

Cheng Shiu University

Thuy Dieu Thi Ung

Institute of Materials Science, Vietnam Academy of Science and Technology

Danh Bich Do

Vinh-Ai Dao

Ho Chi Minh City University of Technology and Education
Yen-Yi Lee
Cheng Shiu University
Guo-Ping Chang-Chien
Cheng Shiu University

Article

Keywords: g-C3N4, atom dispersions, intercalation structures, mono and cluster vacancies, piezo-photocatalysis

Posted Date: December 21st, 2023

DOI: https://doi.org/10.21203/rs.3.rs-3780235/v1

Additional Declarations: There is **NO** Competing Interest.

Version of Record: A version of this preprint was published at Solar RRL on April 1st, 2024. See the published version at https://doi.org/10.1002/solr.202400034.

Abstract

Increasing active sites in catalysts is of utmost importance for catalytic processes, frequently fascinating global scientists. In recent years, using graphitic carbon nitrides (g-C_3N_4) for the piezo-photocatalytic generation of fine chemicals, such as hydrogen peroxide (H_2O_2) from oxygen (O_2) and water (H_2O), is of current interest due to its flexibility in molecular structures to boost catalytic properties. However, due to its intrinsic nature, bulk g-C_3N_4 suffers from low catalytic outcomes. To enhance catalytic performances, we, in this research, engineered g-C_3N_4 by atomically dispersing aluminum (Al) or indium (In) sites to provide catalytic active centers via one-step thermal shock polymerization. The empirical analyses show that In atoms would occupy the near positions of carbon vacancies (V_C) to form N-V_C@In-O bonds. This replacement would produce the highest formation energy based on the theoretical calculations, improving the stability of atom-dispersive materials. In addition, under catalytic conditions, the formation of oxygenic radicals would strongly be associated with the enhanced formation of H_2O_2. Unhappily, hydroxyl radicals would induce catalytic deactivation due to the attacks of these highly oxidative radicals on the active centers, thus changing the catalysts' structures and reducing the catalytic outcomes.

1. Introduction

Over millennia, sunlight has played an irreplaceable role in the life cycle of organisms and humans since it inexhaustibly offers an unlimited energy source. From the early beginning of civilization, people have acknowledged how to employ sunlight for various applications, such as agricultural practices. Conceptually, leveraging sunlight could help surpass current environmental and energy-related issues. However, the intermittent nature of sunlight negatively poses a demeriting point, urgently mandating scientists to pursue advanced technologies to store solar energy. As a result, "solar-to-chemical" conversions have laid a solid foundation to sustain the development of mankind in the chaotic decades [1, 2].

Inspired by natural photosynthesis, in which plants and bacteria can utilize sunlight to convert carbon dioxide (CO_2) and water (H_2O) to oxygen (O_2) and energy in the form of sugar molecules, the great concept of artificial photocatalysis has gradually grown [3]. In 1972, the important discovery by Fujusima and Honda unzipped the ability to produce hydrogen (H_2) from H_2O in the presence of UV-irradiated TiO_2 [4]. This study has drawn scientific attention to light-induced production of fine chemicals. Until now, various small molecules have been synthesized via the photocatalytic process. Among diverse synthesized molecules, hydrogen peroxide (H_2O_2) is irreplaceable to many processes like water purification since highly oxidative hydroxyl radicals (.OH) from decomposing H_2O_2 were majorly associated with removing pollutants to remedy water [5]. Due to its indispensable roles in both academic research and industries, H_2O_2 is strongly expected to be generated from O_2 and H_2O to replace the traditional intensive energy-consuming anthraquinone oxidation methods [6]. Furthermore, H_2O_2 at high concentrations is linked to severe explosion problems, resulting in tremendous concerns about some

safety issues. Therefore, the on-site supplement of dilute H_2O_2 has driven researchers to seek a new solution. In this circumstance, the solar production of H_2O_2 would be an interesting idea to deal with the long inquiries [7].

In photocatalytic processes, photo-responsive materials, called photocatalysts, are used to harvest incident photon energy for driving chemical reactions if the energy is greater or equal to the material's bandgap energy. Followingly, the separation and migration of negative and positive charges might occur, where photogenerated electrons will jump from the material's valance band (VB) to its conduction band (CB) to reduce O_2 directly or indirectly into H_2O_2. Photoexcited holes with high oxidative ability would stay at their VB for other reactions, such as water oxidation. However, the photoexcited electrons and holes tend to recombine rapidly along the way to or on the surface, hampering catalytic performances [8]. To overcome the drawbacks, coupling piezoelectric effects with photocatalysis has currently gained interest from worldwide researchers owing to the potential to defeat charge recombination. Understandably, the non-centrosymmetric essence of materials would benefit the formation of polarization when stressing the material's surfaces with external forces like ultrasound. As a result, thanks to the band-bending phenomenon mechanistically related to the polarization on the catalyst's surfaces, the retardance of electron-hole pair recombination would be achieved to prolong photoexcited charge lifetimes. Hence, the catalytic process would significantly accelerate to maximize its efficiency, evidencing the practical potential of piezo-photocatalysis [9].

In 2019, when Wang and colleagues reported the photo-responsive ability of graphitic carbon nitrides (g-C_3N_4) to produce H_2 from H_2O, the waken-up phenomenon for carbon-based photocatalysts was observed throughout the decades to overcome the ineffectiveness of inorganic semiconductors [10]. From then, various strategies were proposed to improve the catalytic performance of g-C_3N_4 due to the shortcomings of bulk materials, such as low catalytic active sites and limited light absorption capacity. One of the most commonplace methods is introducing metal sites as active centers in g-C_3N_4 structures via doping to enhance adsorption and catalytic processes. Metal ions can help to functionalize g-C_3N_4 frameworks via the coordination between metals and nitrogen to mimic the structure of natural light-responsive compounds, boosting light absorption and charge separation and migration behaviors [11]. Various metals have been discovered and reported in the literature, ranging from alkaline to transition metals [12]. However, most research focused on metals from IA to IIB groups, leaving the gap for metals from IIIA to VA due to the present difficulty. A few studies reported using aluminum (Al) and indium (In) to dope into g-C_3N_4 lattices to improve photocatalytic activities. For instance, Choi and the group fabricated Al-coordinated g-C_3N_4 for H_2 production and water remediation under light irradiation with a facial and scalable synthetic process [13]. Li and co-workers engineered the band energy of g-C_3N_4 with In doping to accelerate charge separation and photocatalytic outcomes [14]. Later, two other consecutive works on In-doped g-C_3N_4 for H_2 evolution were recorded by Yang and co-authors [15, 16]. Most recently, regulating the interlayer distance of g-C_3N_4 by In single atoms via In-N_4 bonds at (002) crystal planes for enhanced CO_2/CO photo-conversion was also reported [17]. Furthermore, doping could

produce the non-centrosymmetric features in g-C_3N_4 due to the structural defects, thus enhancing piezoelectric effects in the material's surfaces to accelerate catalytic results. As exemplified by our previous work, we introduced alkaline-earth metals to g-C_3N_4 lattices to improve piezo-photocatalytic production of H_2O_2, validating the effectiveness of metal-doping in carbon-based materials for piezo-photocatalysis [18]. From these examples, utilizing metals from IIIA groups as a dopant would be an effective strategy to boost the piezo-photocatalytic activity of g-C_3N_4 to produce H_2O_2 from H_2O and O_2, which was not previously observed and reported.

At the beginning of 2023, a group of scientists examined and reported the aggregation of Pt single atoms on TiO_2 under light irradiation [19]. From this research, a question about the stability of metal-doped g-C_3N_4 has been raised. Since metals were mainly decorated into g-C_3N_4 via the coordination with nitrogen, these sites can feasibly be attacked to turn into other forms, such as metal nanoparticles. Such conversions might block the active centers and deactivate the catalysts via altering surface reaction energies. Evidently, Hejazi and colleagues observed clear differences between Pt single atoms and Pt nanoparticles in the photoproduction of H_2 [20]. Despite the uncountable reports on metal-doped g-C_3N_4, a few studies shed light on this regime; hence, it is substantial to examine the piezo-photo stability of these materials, especially for H_2O_2 photoproduction, where the unavoidable presence of O_2 and .OH can convert the metallic active sites to other species, leading to the significant loss of catalytic activities.

With these inspiring studies, our group engineered g-C_3N_4 by introducing Al or In as additional active sites to accelerate the production of H_2O_2 from oxygen reduction reactions (ORR) under light and ultrasound irradiation. On the one hand, we recorded that In-doped g-C_3N_4 and Al-doped g-C_3N_4 can help to enhance the produced amount of H_2O_2, where the catalytic results would be competitive with other existing materials, as shown in Table S1. In addition, the catalytic mechanism was also carefully analyzed and demonstrated the strong dependence on the conversion of oxygen into various types of radicals before manufacturing H_2O_2. On the other hand, In-doped g-C_3N_4 was selected to shed light on the deactivations of the catalysts. The results suggested that In spots in g-C_3N_4 lattices were mainly responsible for the enhancements in catalytic outcomes due to aiding more adsorption sites where the cascade reactions occurred. However, the exposure to O_2 and .OH might convert these sites into other In species, which were believed to block the reactions, leading to low catalytic outcomes. Regarding material perspectives, this research should reinforce the evidence in metal-induced active sites in g-C_3N_4 and demonstrate the possibility of active-site deactivations during piezo-photo treatments, contributing to the deep insights for catalysts' design and development.

2. Results and Discussion

2.1 Piezo-photocatalytic Performance and Electrocatalytic Validations

The catalytic performance of the different prepared catalysts is presented in Fig. 1a. It is obvious that introducing metal elements into g-C_3N_4 frameworks can help accelerate the generation of H_2O_2. Figure 1b also compares photocatalysis, piezo-catalysis, and piezo-photocatalysis by employing ICN as a model catalyst. From the results, only shining light without stirring or sonicating limits the reduction of O_2, leading to a significantly low catalytic outcome. The use of only mechanical forces promoted the reaction yield. Furthermore, combining light and ultrasound considerably enhanced catalytic performance. This phenomenon would originate from the differences in light and ultrasonic intensities in the catalytic systems, which were consistent with our previous reports [18, 21]. Moreover, Ag was decorated on ICN via piezo, photo, and piezo-photodeposition to vividly clarify the impacts between ultrasound and light. The scanning electron microscopy (SEM) and mapping images of Ag-deposited ICN via different methods are shown in Fig. S1 and S2. From the results, most Ag was deposited based on the distribution of In instead of C and N, demonstrating that In spots in g-C_3N_4 lattices act as active centers for adsorption and reduction processes to enhance catalytic properties. It is easy to see that the aggregations of Ag were observed when only UV light was used. At the same time, ultrasound can help to allocate Ag atoms around the surface and avoid Ag aggregations. From this experimental proof, the low H_2O_2 production can be understandable, in which the formation of products around active centers can negatively influence the catalytic performance if only shining light during the reaction due to the blocking effects; thus, the application of external forces like ultrasound is needed to overcome the mass transport limitation phenomenon.

Figure 1c shows the catalytic results of ICN under different gases. Under continuous injection of O_2, the highest catalytic performance was observed in contrast with the presence of other gases. Intriguingly, the formation of H_2O_2 in the N_2-saturated environment would recommend the occurrence of water oxidation to directly or indirectly produce H_2O_2. In addition, various hole scavengers were also applied to estimate the ability to capture excited holes for generating H_2O_2, as shown in Fig. S3a. Without adding methanol (MeOH) and isopropanol (IPA), the production of H_2O_2 was restricted due to the rapid charge recombination, while adding oxalic acid (OA) did not help to improve catalytic performance. However, adding MeOH and IPA meaningfully accelerated the results. Additional radical quenching experiments exhibit the strong dependence of O_2 to H_2O_2 on radical species, as shown in Fig. S3b. From the data, p-benzoquinone (p-BQ), silver nitrate ($AgNO_3$), L-tryptophan (L-tryp), and ethylenediaminetetraacetic acid disodium salt (EDTA.2Na) were employed to trap superoxide $(\cdot O_2^-)$, excited electrons (e^-), single oxygen $^1O_2$, and excited holes (h^+), respectively. From the results, the most impactful radicals in the generation of H_2O_2 were $\cdot O_2^-$ and $^1O_2$ compared with other factors. In addition, nitrotetrazolium blue chloride (NBT) was used to validate further the formation of $\cdot O_2^-$ over time, and the degradation results are presented in Fig. S3c. Fundamentally, NBT can interact with $\cdot O_2^-$ to generate monoformazan, which can trace at 559 nm in UV absorbance spectroscopy [22]. From the data, the degradation of NBT increased with increasing irradiation time, indicating the continuous generation of $\cdot O_2^-$ in the system, which would be

consistent with the in-situ EPR spectra in Fig. 1d. However, the addition of L-tryp into the reaction hindered the removal of NBT, suggesting the competition conversion between NBT and $^1O_2$, where $^1O_2$ would be prioritized.

Further confirmations from the electrocatalytic reduction of O_2 were conducted in this work. Fig. S4 illustrates the ability to reduce O_2 via cyclic voltammetry (CV) and linear sweep voltammetry (LSV) measurements. Moreover, due to the ability to produce H_2O_2 in an inert atmosphere, the other LSV measurements in an anodic direction under darkness and light irradiation were carried out with the data shown in Fig. 1e, Fig. S5a, and Fig. S5b. Obviously, all samples exhibit the ability to evolve O_2 with the positive current observed in the measurements. Besides that, under illumination, the curve shifted to lower overpotential, which could prove the vital role of light in producing O_2 [23]. From these proofs, it is possible to produce H_2O_2 in an inert environment via in-situ oxygen evolution and conversion. The oxygen reduction kinetics were analyzed using Koutecky-Levich plots using rotating disk electrode (RDE) measurements. The results were presented in Fig. 1f, Fig. S5c, and Fig. S5d. All the catalysts show electron transfer (n) values lower than 2, illustrating that the reduction of O_2 would follow dual pathways [24]. Besides, the n values of ICN at all potentials were lower than that of CN and ACN, indicating ICN was towards dual-electron reduction processes, in which the formations of radicals play a pivotal role, as demonstrated in the above section.

2.2 Resolving Catalyst's Structures

In order to determine the crystallization properties of the fabricated catalysts, X-ray diffraction (XRD) measurements were conducted in this study. Notably, the synthesized materials only possess two typical peaks of g-C_3N_4 without any metal oxide or metal nitride features, as presented in Fig. 2a. While the former characteristic at around 13^o was marked with the (100) plane, known as the repetition of heptazine units in g-C_3N_4, the remaining peak, located at 27.4^o represents the interlayer stacking in conjugated systems [18]. The (002) planes of ICN and ACN tend to be recorded at 27.6^o instead of 27.4^o of the CN sample, indicating the intercalation of metal atoms between layers to reduce the interlayer distances owning to stronger electrostatic attraction of metal and non-metal elements [17]. In addition, the presence of ethanol during thermal calcination can cause an increase in the level of doped oxygen into g-C_3N_4, as proved by the data in Table S2. Moreover, ethanol may also induce vacancies in the lattice, reinforcing the right shift in XRD patterns [25]. It is well-known that metal atoms can form coordination bonds with both nitrogen and oxygen, thus leading to the deceleration of interlayer distances between g-C_3N_4.

The BET surface area, pore volume, and pore sizes of the as-prepared materials are summarized in Table S3. It is worth noting that CN possesses the largest BET surface area at 24.34 m^2/g. When Al or In was decorated, the values reduced to 15.21 and 13.29 m^2/g for ACN and ICN, respectively, illustrating the occupancy of metallic atoms in CN structures. The lower BET surface area of ICN compared to ACN was induced by a larger percentage of In compared to Al, as analyzed by ICP-MS and shown in Table S2.

Moreover, the increase in average pore size was recorded when adding $AlCl_3$ or $InCl_3$ during the calcination process. It validates that the decomposition of molten salts could help to generate big pore sires, as previously observed in our publication [18]. Although CN shows the largest surface area compared to ACN or ICN, the catalytic performance of these samples exhibited a stark contrast. This would evidence the roles of metal in the modified samples, in which reactants will be adsorbed and reduced at these sites.

Figure 2b displays the FTIR spectra of the as-prepared catalysts with the typical features for g-C_3N_4 structures. In particular, the sharp band at 810 cm^{-1} depicts the breathing mode of heptazine units [27]. The multi-peaks ranging from 1200 to 1700 cm^{-1} were associated with the mode of C = N and C-N bonds in the heterocycles, whereas the regions from 3000 to 3300 cm^{-1} indicate the presence of O-H and N-H bonds [28]. Generally, when comparing the FTIR intensity of ICN to other samples, ICN presents a weak intensity in all regions, suggesting ICN would contain more structural defects since the formation of coordination bonds alters the vibration of the local environment. Further structural characterizations were shown in Fig. 2c by employing solid-state NMR spectroscopy. From the ^{13}C NMR spectra, three samples exhibit two typical shifts at 158 and 165.8 ppm, corresponding to C-$(N)_3$ and -N = C(N)-NH_2 groups in g-C_3N_4 structures [29]. Additionally, the small signal at 165.1 ppm was assigned to C-O-C species, which would be believed to enhance the catalytic properties in ORR [30]. Regarding the NMR intensity, ACN exhibits a lower signal than CN in contrast with ICN, where a higher signal is recorded. This result suggests the different behaviors of Al and In atoms in g-C_3N_4. Particularly, In atoms tend to bridge g-C_3N_4 layers via coordination bonds to support the growth of g-C_3N_4 units, while Al doping damages the structures as certified by XRD patterns. In the case of ICN, although In atoms intercalate to connect g-C_3N_4 layers, the difference in stacking direction would reduce the crystallinity, resulting in a lower XRD intensity at the (002) plane.

Furthermore, X-ray photoelectron spectroscopy (XPS) was carried out to characterize the surface properties of the materials. As shown in Fig. S6a, the survey spectra display the presence of carbon, nitrogen, and oxygen. Additionally, the unobservable features of Al 2p and In 3d on the survey spectra indicate a very high level of metal dispersion on the g-C_3N_4 surfaces [31]. The high-resolution XPS spectra of Al 2p and In 3d are depicted in Fig. S6b and S6c, with distinct signals of the oxidation state of + 3 for these metals. In Fig. S6d, C 1s spectra exhibited five deconvoluted peaks at around 284.8, 286.6, 287.9, 289.5, and 294 eV, which can be assigned to C-C, C-N, N = C-N, O = C-O, and π-$π^*$ bonds, respectively, in the materials [32, 33, 34]. The high-resolution spectra of N 1s in Fig. S6e reveal the presence of C = N-C, N-$(C)_3$, C-N-H, and π-$π^*$ bonds. While these peaks for ICN were located at 398.8, 400, 400.9, and 404.6 eV, the shifting to higher binding energy was observed for ACN and CN, with these peaks being situated at 399.9, 401.6, 402.3, and 405.9 eV, respectively [34, 35]. The shifting in the N 1s spectra of ICN compared to CN and ACN would be associated with the level of defects in ICN, indicating that the defects happen at nitrogen sites to reduce the binding energy of these nitrogen species. In O 1s spectra in Fig. S6f, there are three convoluted peaks located at 531.5, 532.6, and 533.3 eV, corresponding

to C-O-H, O-H adsorbed from moisture, and C-O-C bonds on the material's surface [39, 40]. In addition, the calculated area ratio between N-$(C)_3$ and C-N-H from XPS peak areas, presented in Fig. S7a, witnesses a larger concentration of amino groups on the ACN and ICN surfaces compared to CN [37]. This functional group can be clarified as one of the quintessential structural defects in g-C_3N_4 surfaces due to incomplete polymerization. It is pointed out that the large amount of primary amine moieties would be towards water production from ORR, reducing the selectivity of H_2O_2, which will hamper catalytic outcomes [38]. However, this study observed the stark contrasting phenomenon, recommending that Al and In coordinate with nitrogen from these groups to provide active sites, in which the selectivity towards H_2O_2 was improved to accelerate the catalytic performance.

Energy-dispersive X-ray spectroscopy (EDS) was employed to determine the C/N ratio in the bulk form of the materials. The elemental distribution images of as-prepared catalysts are illustrated in Fig. S8a, b, and c, while Fig. 8d, e, and f present the EDS spectra of the catalysts. As presented in Fig. S7b, there are no distinct differences in the bulk ratio of the synthesized materials, while the surface ratio, calculated from XPS data, manifests the highest value for ACN. The data suggests that ACN has some point defects in enriching the number of carbon atoms in contrast to the enrichment of nitrogen atoms of ICN. Due to this reason, the amount of Al in the materials is smaller than that of In because of inadequate coordinating sites.

Solid-state EPR spectra were recorded to assess the level of vacancies in the prepared samples. Figure 1d recommends that CN tends to possess more nitrogen vacancies in the lattices, whereas ACN and ICN would have more carbon vacancies. However, EPR spectra are unable to distinguish cluster vacancy species. Thus, positron annihilation spectroscopy (PAS) was also used to validate the vacancy properties of the materials. The positron annihilation lifetime (PAL) analyses of all samples are presented in Table S4. Two positron lifetime components were obtained for three samples. The first (shortest) lifetime (τ_1) is known to be originated from the combined annihilation of positrons with electrons in perfect structure and monovacancies of N (V_N), whereas the second lifetime (τ_2) is attributed to the positron annihilation in vacancy clusters, which contain both V_N and V_C [40, 41]. A slight reduction of τ_1 was seen for two doped ACN (τ_1 ~ 0.130 ns) and ICN (τ_1 ~ 0.131 ns) samples compared to the original CN (τ_1 ~ 0.136 ns) one. This reduction of τ_1 indicated a slight reduction of V_N concentration in those doped samples due to the occupation of O atoms to the V_N sites in the g-C_3N_4 structure under rich-oxygen synthetic conditions. However, all obtained τ_1 values are lower than that previously reported for V_N-rich g-C_3N_4 (τ_1 ~ 0.156 ns) [42]. This means that those samples should be constructed more favorably to heptazine-based g-C_3N_4-h structure (high electron density) than triazine-based (gC_3N_4-t) one (low electron density) because the positron lifetime is known to be inversely proportional to average electron density in the cell unit of structure and to the concentration of V_N as well [43, 44]. As for the second-lifetime component τ_2, which relates to the presence of vacancy clusters, one can see that the CN sample should contain vacancy clusters formed by $3V_C + 2V_N$ as its τ_2 value (0.358 ns) is close to that calculated for the same vacancy cluster in the same material [41]. Similarly,

ACN (τ_2 ~ 0.360 ns) and ICN (τ_2 ~ 0.363 ns) should have vacancy clusters of $4V_C + 2V_N$, which are one V_C higher than that of CN due to their higher τ_2 values.

Because of the competitive annihilations of positrons with electrons in a perfect structure, V_N, and vacancy clusters, it would be difficult to evaluate the total concentrations of defects in the samples based on the annihilation intensities ($I_{1,2}$) in Table S4. In such a case, DB analysis was utilized. Fig. S9a shows that the value of S parameter, which is sensitive to the total concentration of defects, obtained for the CAN and ICN samples is much higher than that obtained for CN. This result means that the doping process should not only reduce the V_N concentration, as indicated by PAL analysis, but also enhance the formation of new defects associated with a complex mix of dopants versus defects systems. This is confirmed by looking closely at the correlated plot of S and W parameters in Fig. S9a, which shows that ACN and ICN should have the same defect types (those samples are on the linear line), whereas CN has a different type of defects (this sample is out of the linear line). This result also reveals that doped Al and In atoms should have successfully modified the structure of g-C_3N_4 by their interaction with defective sites.

To gain insight into the sites of the dopants in modified g-C_3N_4 structures, EMD analyses were conducted using CN and single-crystal Si samples for references, as shown in Fig. 1e and Fig. S9b, respectively. Fig. S9b shows that for the CN sample, two EMD peaks at electron momenta P_L ~ 10.8×10^{-3} m_oC and 12.9×10^{-3} m_oC are associated, respectively, with the positron annihilations with $e_C(2p)$ and $e_N(2p)$ were observed [40, 42, 45]. Those EMD peaks reflect the existence of both V_N and V_C in CN, but the concentration of V_C should be higher than that of V_N due to the enhanced strength of the EMD peak at P_L ~12.9×10^{-3} m_oC compared to that at P_L ~10.8×10^{-3} m_oC. This observation reconfirms the formation of V_C-rich vacancy clusters indicated by the above PAL analysis. For ACN and ICN, there appeared a new EMD peak at P_L ~ 12.0×10^{-3} m_oC due to the positron annihilation with $e_{In}(4d)$ in the ICN sample [46]. At the same time, there also appeared a right shift of the EMD peak position from P_L ~ 12.9×10^{-3} m_oC to ~ 13.2×10^{-3} m_oC as well as a reduction of EMD peak associated with the positron annihilations with $e_N(2p)$ in both ICN and ACN. These results indicated that doped Al and In atoms should strongly interact with V_C in vacancy clusters of ICN and ACN, respectively. To clarify this indication, EMD curves obtained using CN reference in Fig. 1e were analyzed. In Fig. 1e, EMD curve of ICN exhibits the simultaneous appearance of positron annihilations with $e_O(2p)$ (P_L ~ 10.0×10^{-3} m_oC), $e_N(2s)$ (P_L ~ 19.0×10^{-3} m_oC), $e_{In}(4d)$ (P_L ~ 12.0×10^{-3} m_oC), and $e_{In}(5s)$ (P_L ~ 6.2×10^{-3} m_oC), which cannot be clearly seen in Fig. S9b [42, 46, 47]. This result is extremely interesting as it clearly revealed that positrons were trapped in a complex system of N-V_C@In-O, or in other words, a complex system of N-V_C@In-O had been formed. In this system, because the atomic radius of In is larger than that of C, In should be located on the top of V_C instead of occupying V_C, which allows it to participate in the layered structure formed by two ICN layers [48]. Furthermore, the strongest enhancement of positron annihilations with $e_{In}(5s)$ obtained for ICN indicated that In should be bonded with two N and one O

atoms of the V_C-contained layer and two N atoms of the remaining layer to form a single-atom structure of N-V_C@In-O in the heptazine units, instead of the empty space between them. Such a formation could not be seen for the ACN sample, implying that almost Al could be in different forms in the empty space between the heptazine units.

The above analyses would meaningfully validate the unique structures of ICN. Thus, density functional theory (DFT) calculations on orthorhombic CN unit cell models were further applied to confirm the experimental data. Figure 1f illustrates the side view of the optimized ICN structure, highlighting a significant elevation of the In atom positioned at the center of the interlayer within the (002) crystal plane. This In atom establishes bonds with O and the four nearest N atoms, distributing itself across both upper and lower CN layers. The emergence of this unique five-fold bonding pattern can be ascribed to two key factors: (i) the relatively large size of In, hindering its facile embedding into the surface, and (ii) the versatility of In atoms to manifest multiple oxidation states, such as from + 1 to + 3^3, facilitating binding with numerous neighboring atoms. Notably, the presence of the In atom induces substantial corrugation in the CN layers. This corrugation is particularly pronounced in the upper and lower layers adjacent to the In atom, with roughness coefficients of approximately 0.3 and 0.5 Å, respectively. These distinctive structural characteristics contribute to an enhanced specific surface area for ICN compared to CN, consequently elevating its catalytic performance. The calculations indicate that ICN is significantly stable, with the defect formation energy (E_f) being highly endothermic (~ -6.0 eV). In comparing the E_f to other defects, such as single O_N and In_C, and even to the other ICN isomer where the In is assumed to be at the center of the triazine unit in the CN lattice, our results suggest that the ICN configuration is energetically more stable, underscoring its relevance to experimental measurements.

The zeta potential measurements were also conducted in the study to determine the surface charges of the synthesized materials. The results are summarized in Table S3, with all samples exhibiting negative surface charges, which might be believed to benefit the proton adsorption for boosting the process efficiency. Furthermore, transmission electron microscopy (TEM) images in Fig. S10 demonstrate the morphological features of the as-prepared materials. All samples exhibit 2D nanosheet structures. While CN and ICN exhibit fewer defective structures, ACN appears to have many porous features. These results provide meaningful proof to certify the point from NMR analyses, where In atoms help to connect layer structures without damaging the nanosheets. Additionally, to catch the presence of In single atoms and clusters in g-C_3N_4, scanning transmission electron microscopy (STEM) was utilized in the work. Figure 1g and S11 show the STEM image of ICN with the appearance of some In atoms and clusters on g-C_3N_4 surfaces. From Fig. 1g, the elemental mapping image of ICN is presented with the dense distribution of C, N, and O around In atoms, vividly illustrating more evidence for the formation of N-V_C@In-O in the system, as following the other characterizations.

2.3 Role of Defects in Charge Separation and Migrations

In order to fully assess the light-responsive properties of the synthesized materials, ultraviolet-visible diffuse reflectance spectroscopy (UV DRS) was employed in the work, and the data are presented in

Fig. 3a. From the results, it is critical to see that CN exhibits lower light absorption ability compared to ACN and ICN; thus, validating the point that adding metal sites can extend and improve the responses of the materials with light, accelerating catalytic outcomes. Additionally, photoluminescence (PL) spectroscopy was also applied to study the charge recombination of the materials. The spectra are demonstrated in Fig. S12, with the data supplementing that modified samples have lower electron-hole recombination properties compared to pristine CN. It is well-known that the charge recombination can be terminated by the defective states in the materials. Therefore, the PL energy spectra are provided in Fig. 3b with four deconvoluted peaks at around 2.48, 2.54, 2.69, and 2.82 eV representing the defective states, π^*-π, π^*-LP, and σ^*-LP of the materials where LP is the lone pair state [21]. From this result, the defective percentage can be roughly exported via the area ratio between the defective states and the whole spectra area, with the calculated values for CN, ACN, and ICN being 20.2, 49.6, and 45.3 %, rspectively. It is not difficult to see that ACN and ICN possess more defects than CN, which could help to quench the charge recombination during light irradiation, meaningfully boosting the catalytic outcomes. From the UV and PL analyses, the additions of metal active centers in the materials would create more defects in the materials, resulting in the extent of light absorption ability and enhancement in quenching rapid charge recombination.

Followingly, the bandgap energy of the prepared materials was exported via a Kubella-Munk model, with the data being 2.67, 2.65, and 2.62 eV for CN, ACN, and ICN, respectively, as presented in Fig. S13a. The midgap state was also computed at 1.80, 1.55, and 1.66 eV for CN, ACN, and ICN sequentially. The midgap state opens more channels for charge excitations under lower photon energy compared to the main channel, leading to higher catalytic activities [49]. To determine the location of the valance band (VB), XPS-VB spectra were recorded, and the analytic data are presented in Fig. S13b. The results show that CN, ACN, and ICN exhibit the VB maximum (VBM) at 2.48, 2.39, and 2.41 eV, respectively. Via calculations, the VB positions of CN, ACN, and ICN are determined at 1.92, 1.83, and 1.85 eV. The electron states lower than VBM in the XPS-VB results were associated with the redistribution of extra electrons in the conjugated systems due to the presence of vacancy species [50]. Furthermore, Mott-Schottky plots were provided in Fig. S13c, S13d, and S13e for CN, ACN, and ICN to validate the conduction band (CB) positions of the analyzed materials. All samples exhibit a positive slope, which can be featured as an n-type semiconductor. The charge carrier densities were also calculated in the work. The data from Table S5 illustrates that the addition of metal into g-C_3N_4 would improve the charge carrier densities of the materials, helping to accelerate catalytic outcomes. The whole calculated data for band structures of the synthesized materials are synopsized in Table S5, and Fig. 3c demonstrates the diagram for the material's band positions. As can be seen in the diagram, all samples depict the ability to generate H_2O_2 via different pathways, including water oxidation and oxygen reduction.

Moreover, due to the unique structures of ICN, the DFT calculations were applied to unravel the electronic structures of the materials to get more insights into the experimental data. Fig. S13f highlights the alteration in the bandgap of ICN compared to pristine CN. The electronic structure reveals that ICN's band gap is smaller than CN by approximately 0.78 eV. The confidence in the theoretical predictions is

substantiated by estimating CN's band gap to be around 2.99 eV, closely aligning with the optical band gap of 2.67 eV measured using UV-vis spectroscopy. The narrowing of ICN's band gap to 2.21 eV implies higher photo-absorption efficiency compared to pristine CN, thereby increasing the photocatalysis efficiency for water splitting, as observed in the experimental measurements mentioned above. Notably, the calculated bandgap energy of ICN was lower than that from the experimental data since the model proposed the perfect layers in contrast with the synthesized materials. To comprehend the origin of the bandgap reduction, the (projected) density of state analysis [(P)DOS] of the ground-state electronic structures was conducted further. As illustrated in Fig. S13g, it reveals that the presence of the O-In complex defect in ICN significantly lowers the position of the conduction band minimum (CBM) and slightly elevates the valence band maximum (VBM) relative to those in pristine CN. The impacts of the O-In complex on these changes, however, are indirect, with the In atom breaking the symmetry of the N atoms nearest to In, giving rise to defect-like states resembling the N-p orbitals. This is particularly evident for N1 and N3 atoms, as shown in the inset of Fig. S13g. Orbitals of these new defect states differ from the hybrid sp^2-like orbital characterizing the pristine CN's CBM state.

Eventually, the photo, piezo, and piezo-photo responsive properties of the synthesized materials were analyzed. Figure 3d shows the transition photocurrent under the on-off cycles of the synthesized materials, in which ACN postulates the highest current under illumination compared to CN and ICN. It is believed that the transition photocurrent was impacted by the surface defects of the materials. Thus, when comparing the current between CN and ICN, ICN tends to have lower photocurrent due to the number of defects on the surfaces, which play as an electron pool to store excited charges [51]. From this result, ACN and ICN would have different defect types in their structures, which could behave differently in catalytic processes. Furthermore, the results from electrochemical impedance spectroscopy (EIS) under light irradiation in Fig. S14a also validate the roles of defects in the modified materials [52]. Abnormally, the Nyquist radii of ACN and ICN are bigger than that of CN, implying that the charge separation and migration efficiency of ACN and ICN are lower than that of CN owing to the presence of different defects. However, the catalytic outcomes and other characterizations of these samples are in the opposite direction, indicating the defect locations would be the main active sites for the catalytic reactions in which the adsorption and oxidation or reduction processes happen. Additionally, the charge carrier lifetime (τ_e) of all samples was calculated from the EIS Bode plot in Fig. S14b, with the data being 0.899, 1.023, and 1.164 ms. The results show that adding the metal centers to the materials can help enhance the charge carrier lifetime of the pure materials, which would help accelerate catalytic performance.

Additionally, to examine the piezoelectric properties of the prepared materials, piezo-response force microscopy (PFM) was utilized in the research. Figure 3e and 3f illustrate the height and amplitude images of the ICN sample. The characterized data of CN and ACN are depicted in Fig. S15. All samples exhibit the piezoelectric properties in the characterization. The butterfly loops of CN, ACN, and ICN under a 10-bias field were also provided in this work via Fig. S15 and Fig. 3g. From the amplitude signals, ACN and ICN perform higher signals than CN, indicating the better piezo catalytic properties of the modified

samples [53] Moreover, it is believed that water flow can induce piezoelectric effects in the materials [54]. Thus, to scrutinize the piezo-photoelectric properties of the catalysts, the EIS measurements under rotation and light irradiation were implemented in this work. Notably, this study utilized rotation instead of ultrasound to study piezoelectric effects to avoid noise from ultrasound under electrochemical measurements. Figure 3h demonstrates better charge separation and migration under rotating conditions, in which the Nyquist radius of ICN was smaller in the case of light illumination. From Fig. S16, all the EIS results of CN, ACN, and ICN are postulated where the rotating-speed dependence is shown. Increasing rotating speeds improves the piezo-photoelectric effects, recommending better catalytic outcomes.

2.4 Structural Evolution under Irradiation

Stability is one of the most essential parameters for catalytic studies. Thus, the stability of ICN over six cycles running with different saturated atmospheres was implemented in the research. The stability data are shown in Fig. 4a. From the results, over six cycles, the catalytic performance of ICN was reduced by roughly 15% in all examined environments. The XRD patterns of ICN before and after catalysis were recorded to understand the phenomenon. Figure 4b demonstrates the XRD patterns of ICN before and after six cycles of working under the nitrogen and air-saturated solutions. It is easy to see that the intensity at the (002) plane of ICN increases after use, confirming the decrease in the structural defects to improve the crystallinity of the materials. The additional observation is that the spacing distance between two g-C_3N_4 layers increases, which would be associated with the damage of unique structures of ICN. The same phenomenon was observed in the oxygen-saturated solution with more detailed information, as shown in Fig. 4c. After catalysis, the observation of InN and $In(OH)_3$ peaks in the XRD patterns would illustrate the presence of N-In and In-O bonds in the ICN systems. Interestingly, the XRD intensity after four and five cycles increases compared to that of ICN before use. However, the intensity reduces after six cycles, suggesting severe changes in the ICN structures. In order to reveal the reasons for the structural changes, in-situ EPR spectra were applied to probe the formation of hydroxyl radicals (.OH), which are highly oxidative and can attack the active centers to damage the unique structures of ICN. Figure 4d confirms the ability to form .OH in catalytic conditions. As mentioned before, the band locations of ICN would not be able to oxidize water to produce this radical. Thus, these radicals would originate from the decomposition of generated H_2O_2 in the solution and attack the In centers to deactivate the catalysts. From the results, the oxygen-saturated environment would encourage the formation of H_2O_2, while the amount of .OH will also increase in the solution to cleave the chemical bonds between In and local elements, prompting the catalytic deactivation phenomenon.

3. Conclusion

Briefly, this work introduced the direct calcination to atomically disperse In and Al on g-C_3N_4 to add more active sites to enhance the production of H_2O_2 via piezo-photocatalysis. The data revealed the unique structures of N-V_C@In-O bonds in g-C_3N_4 lattices, which would help enhance light absorption, piezoelectric potentials, and charge transport behaviors. In addition, the synthesized catalysts exhibit an

excellent catalytic performance over several cycles. However, the formation of hydroxyl radicals via H_2O_2 decomposition in the solution leads to the structural deterioration of ICN, inducing reduced catalytic activity. This work sheds light on the effectiveness of metal on supporting materials and gives insights into the deactivation of catalysts in highly oxidative environments. Thus, it would motivate further studies to rationally design the materials with anti-poisoning effects of hydroxyl radicals, which can help to accelerate the use of piezo-polarized photocatalysts for solar H_2O_2.

4. Synthesis of g-C3N4 and modified samples

In the typical preparation, g-C_3N_4 and its derivatives were synthesized via thermal polymerization. Specifically, 4 g of melamine, 4 g of dicyandiamide, and 0.25 g of XCl_3 (X: Al or In) were ground for a while to get homogeneity. Afterward, 5 mL of ethanol was poured into the prepared powders to obtain a cream-like mixture before calcinating at 550 ^oC in an ambient atmosphere for 4 h. Then, the calcinated powders were collected, ground, and immersed in 0.25 M of an aqueous H_2SO_4 solution for roughly 24 h to remove metal oxides on the surface of the catalysts prior to washing and drying to attain final samples, which were stored for further uses. The samples were noted as ACN or ICN with the addition of $AlCl_3$ or $InCl_3$, while CN was denoted as a bare sample without adding salts.

Declarations

Acknowledgments

We acknowledge Ho Chi Minh City University of Technology (HCMUT), VNU-HCM, and Prof. Phung K. Le for supporting this study. Hoai-Thanh Vuong thanks the support from the Vingroup Science and Technology Scholarship program and the UCSB Chancellor Fellowship. This works associated with positron annihilation analysis are supported by the National Foundation for Science and Technology Development (NAFOSTED) of Vietnam through Grant No. 103.02-2023.20. The theoretical simulations in this work are performed using HPC Systems of Phenikaa University.

Conflict of Interest

The authors declare no conflict of interest.

Data Availability Statement

The data that support the findings of the study are available from the co-responding authors upon the reasonable request.

Supporting Information

Supporting Information is available from the authors and is accompanied by this work.

References

1. Q. Wang, K. Domen, *Chem. Rev.*, **2020**, *120*, 919-985.
2. H.-T. Vuong, D.-V. Nguyen, L. P. Phuong, P. P. D. Minh, B. N. Ho, H. A. Nguyen, *Carbon Neutralization*, **2023**, 1-33.
3. E. Romero, V. I. Novoderezhkin, R. v. Grondelle, *Nature*, **2017**, *543*, 355-365.
4. A. Fujishima, K. Honda, *Nature*, **1972**, *238*, 37-38.
5. S. Gligorovski, R. Strekowski, S. Barbati, D. Vione, *Chem. Rev.*, **2015**, *115*, 13051-13092.
6. H. Hou, X. Zeng, X. Zhang, *Angew. Chem. Int. Ed.*, **2020**, *59*, 17356-17376.
7. Y. Sun, L. Han, P. Strasser, *Chem. Soc. Rev.*, **2020**, *49*, 6605.
8. Z. Chen, D. Yao, C. Chu, S. Mao, *Chem. Eng. J.*, **2023**, *451*, 138489.
9. S. Tu, Y. Guo, Y. Zhang, C. Hu, T. Zhang, T. Ma, H. Huang, *Adv. Funct. Mater.*, **2020**, *30*, 2005158.
10. X. Wang, K. Maeda, A. Thomas, K. Takanabe, G. Xin, J. M. Carlsson, K. Domen, M. Antonietti, *Nature Mater.*, **2009**, *8*, 76-80.
11. X. Wang, X. Chen, Arne Thomas, Xianzhi Fu, Markus Antonietti, *Adv. Mater.*, **2009**, *21*, 1609-1612.
12. L. Jiang, X. Yuan, Y. Pan, J. Liang, G. Zeng, Z. Wu, H. Wang, *Appl. Catal.* B, **2017**,*217*, 388-406.
13. C. H. Choi, L. Lin, S. Gim, S. Lee, H. Kim, X. Wang, W. Choi, *ACS Catal.*, **2018**, *8*, 4241-4256.
14. H. Li, Y. Xia, Z. Liang, G. Ba, W. Hou, *ACS Appl. Energy Mater.*, **2020**, *3*, 377-386.
15. X. Yang, Z. Guo, X. Zhang, Y. Han, Z. Xue, T. Xie, W. Yang, *New J. Chem.*, **2021**, *45*, 544, 2021.
16. X. Yang, C. Cao, Z. Guo, X. Zhang, Y. Wang, W. Yang, *New J. Chem.*, **2021**, *45*, 7231, 2021.
17. C. Ding, X. Lu, B. Tao, L. Yang, X. Xu, L. Tang, H. Chi, Y. Yang, D. M. Meira, L. Wang, X. Zhu, S. Li, Y. Zhou, Z. Zou, *Adv. Funct. Mater.*, **2023**, *33*, 2302824.
18. H.-T. Vuong, D.-V. Nguyen, P. P. Ly, P. D. M. Phan, T. D. Nguyen, D. D. Tran, P. T. Mai, N. H. Hieu, *ACS Appl. Nano Mater.*, **2023**, *6*, 664-676.
19. N. Denisov, S. Qin, J. Will, B. N. Vasiljevic, N. V. Skorodumova, I. A. Pašti, B. B. Sarma, B. Osuagwu, T. Yokosawa, J. Voss, J. Wirth, E. Spiecker, P. Schmuki, *Adv. Mater.*, **2023**, *35*, 2206569.
20. S. Hejazi, S. Mohajernia, B. Osuagwu, G. Zoppellaro, P. Andryskova, O. Tomanec, S. Kment, R. Zborˇil, P. Schmuki, *Adv. Mater.*, **2020**, *32*, 1908505.
21. D. D. Tran, H.-T. Vuong, D.-V. Nguyen, P. P. Ly, P. D. M. Phan, V. H. Khoi, P. T. Mai, N. H. Hieu, *Nanoscale Adv.*, **2023**, *5*, 2327.
22. H.-Y. Liu, C.-G. Niu, D.-W. Huang, C. Liang, H. Guo, Y.-Y. Yang, L. Li, *Chem. Eng. J.*, **2023**, *465*, 143007.
23. C. Ye, J.-X. Li, Z.-J. Li, X.-B. Li, X.-B. Fan, L.-P. Zhang, B. Chen, C.-H. Tung, L.-Z. Wu, *ACS Catal.*, **2015**, *5*, 6973-6979.
24. Y. Pan, X. Liu, W. Zhang, B. Shao, Z. Liu, Q. Liang, T. Wu, Q. He, J. Huang, Z. Peng, Y. Liu, C. Zhao, *Chem. Eng. J.*, **2022**, *427*, 132032.
25. Y. Zhu, H. Zhang, H. Liu, G. He, X. Liu, J. Xiao, Y. Sun, L. Han, *Chem. Commun.*, **2022**, *58*, 10084.

26. S. Stefa, M. Griniezaki, M. Dimitropoulos, G. Paterakis, C. Galiotis, G. Kiriakidis, E. Klontzas, M. Konsolakis, V. Binas, *ACS Appl. Nano Mater.*, **2023**, *6*, 1732-1743.
27. Z. Tong, Y. Hai, B. Wang, F. Lv, Z. Zhong, R. Xiong, *J. Phys. Chem. C*, **2023**, *127*, 11067-11075.
28. S. Samanta, R. Yadav, A. Kumar, A. K. Sinha, R. Srivastava, *Appl. Catal. B*, **2019**, *259*, 118054.
29. V. R. Battula, B. Rawat, K. Kailasam, *ACS Appl. Polym. Mater.*, **2023**, *5*, 1989-1997.
30. P. Ren, T. Zhang, N. Jain, H. Y. V. Ching, A. Jaworski, G. Barcaro, S. Monti, J. Silvestre-Albero, V. Celorrio, L. Chouhan, A. Rokicinska, E. Debroye, P. Kustrowski, S. V. Doorslaer, S. V. Aert, S. Bals, S. Das, *J. Am. Chem. Soc.*, **2023**, *145*, 16584-16596,.
31. S. Wang, H. Zhang, R. Nie, Y. Ning, C. Zhao, Z. Xia, P. Niu, L. Li, S. Wang, *Dalton Trans.*, **2022**, 51, 13015.
32. Y. Zheng, Y. Liu, X. Guo, Z. Chen, W. Zhang, Y. Wang, X. Tang, Y. Zhang, Y. Zhao, *J. Mater. Sci. Technol.*, **2020**, *41*, 117-126,.
33. T. T. Dang, T. K. A. Nguyen, K. C. Bhamu, T. Mahvelati-Shamsabadi, V. K. H. Van, E. W. Shin, K.-H. Chung, S. H. Hur, W. M. Choi, S. G. Kang, J. S. Chung, *ACS Catal.*, **2022**, *12*, 13763−13780.
34. H. Liu, D. Chen, Z. Wang, H. Jing, R. Zhang, *Appl. Catal. B*, **2017**, *203*, 300-313.
35. Q. Li, Y. Jiao, Y. Tang, J. Zhou, B. Wu, B. Jiang, H. Fu, *J. Am. Chem. Soc.*, **2023**, *145*, 20837-20848.
36. Y. Zhang, Z. Chen, J. Li, Z. Lu, X. Wang, *J. Energy Chem.*, **2021**, *54*, 36-44,.
37. F. Wei, Y. Liu, H. Zhao, X. Ren, J. Liu, T. Hasan, L. Chen, Y. Li, B.-L. Su, *Nanoscale*, **2018**, *10*, 4515.
38. J. S. Kim, J. W. Oh, S. I. Woo, *Catal. Today*, **2017**, *293-294*, 8-14,.
39. Y. Shiraishi, Y. Kofuji, H. Sakamoto, S. Tanaka, S. Ichikawa, T. Hirai, *ACS Catal.*, **2015**, *5*, 3058-3066,.
40. T. Kashyap, P. J. Boruah, H. Bailung, D. Sanyal, B. Choudhury, *Nanoscale Adv.*, **2021**, *3*, 3260.
41. P. Praus, L. Řeháčková, J. Čížek, A. Smýkalová, M. Koštejn, J. Pavlovský, M. F. Edelmannová, K. Kočí, *Sci. Rep.*, **2022**, *12*, 13622.
42. B. Choudhury, K. K. Paul, D. Sanyal, A. Hazarika, P. K. Giri, *J. Phys. Chem. C*, **2018**, *122*, 9209-9219.
43. M. R. Fiorentin, F. Risplendi, M. Palummo, G. Cicero, *ACS Appl. Nano Mater.*, **2021**, *4*, 1985-1993.
44. F. Tuomisto, I. Makkonen, *Rev. Mod. Phys.*, **2013**, *85*, 1583.
45. A. Sachdeva, K. Sudarshan, P.K. Pujari, A. Goswami, K. Sreejith, V.C. George, C.G.S. Pillai, A.K. Dua, *Diam. Relat. Mater.*, **2004**, *13*, 1719-1724.
46. M. Elsayed, T. E. M. Staab, J. Cížek, R. Krause-Rehberg, *Acta Mater.*, **2021**, *219*, 117228.
47. M. Chakrabarti, A. Banerjee, D. Sanyal, M. Sutradhar, A. Chakrabarti, *J. Mater. Sci.*, **2008**, *43*, 4175-4181.
48. B. K. Vainshtein, V. M. Fridkin, V. L. Indenbom , *Spinger*, Berlin, **1995**.
49. J.-Y. Tang, X. Y. Kong, B.-J. Ng, Y.-H. Chew, A. R. Mohamed, S.-P. Chai, *Catal. Sci. Technol.*, **2019**, 9, 2335.
50. P. Niu, G. Liu, H.-M. Cheng, *J. Phys. Chem.* C, **2012**, *116*, 11013-11018.
51. J. Shi, H. Cui, Z. Liang, X. Lu, Y. Tong, C. Su, H. Liu, *Energy Environ. Sci.*, **2011**, *4*, 466-470.

52. Y. Zhu, Q. Ling, Y. Liu, H. Wang, Y. Zhu, *Appl. Catal. B*, **2016**, *187*, 204-211.
53. P. Wang, S. Fan, X. Li, J. Duan, D. Zhang, *ACS Catal.*, **2023**, *13*, 9515-9523.
54. Y. Zhang, L. Wang, H. Huang, C. Hu, X. Zhang, C. Wang, Y. Zhang, *Appl. Catal. B*, **2023**, *331*, 122714.

Figures

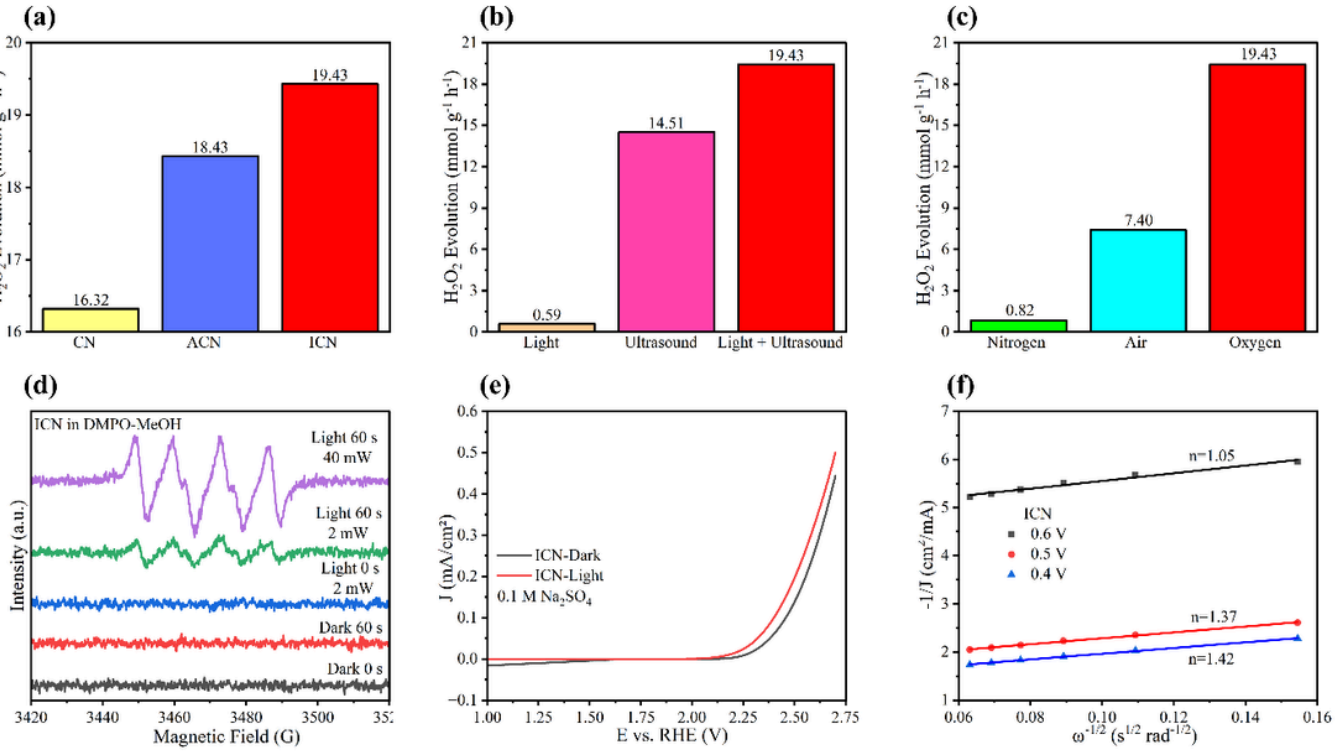

Figure 1

Catalytic performance of different samples (a); Photocatalytic, piezo-catalytic, and piezo-photocatalytic performance of ICN (b); Catalytic performance of ICN under nitrogen (N_2), air, and oxygen (O_2) (c); In-situ electron paramagnetic resonance (EPR) spectra of ICN under dark and light irradiation (d); Polarization curves of ICN under darkness and light irradiation (e); and Koutecky-Levich (K-L) plots from ICN (f)

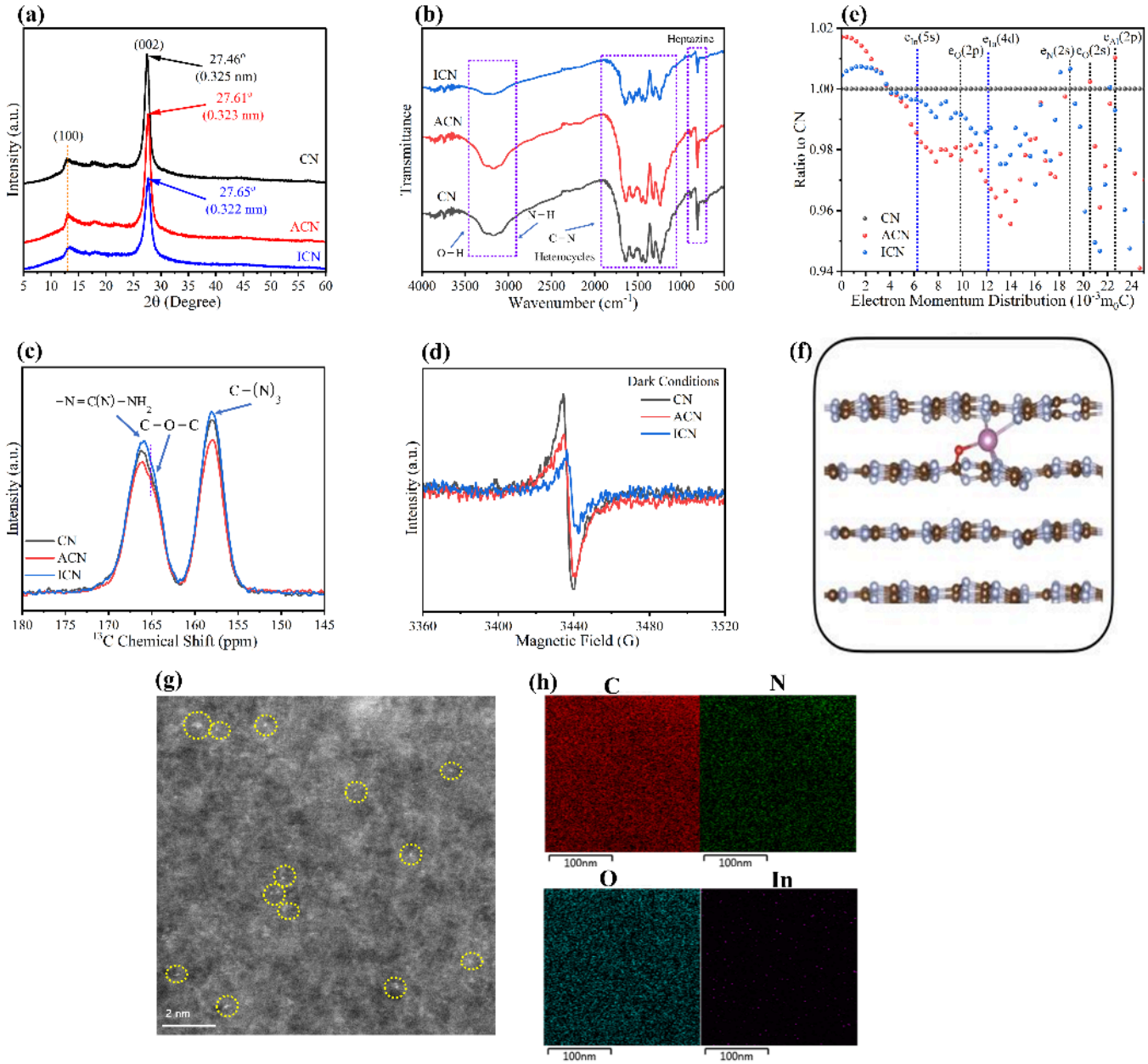

Figure 2

XRD patterns of the prepared catalysts (a); FTIR spectra of the studied catalysts (b); ^{13}C solid-state NMR spectra of the synthesized materials (c); solid-state EPR spectra of CN, ACN, and ICN(d); Electron momentum distributions (EMD) analyzed using original CN references, dotted lines with $e_C(2p)$, $e_{In}(4d$ or $5s)$, $e_O(2p)$, $e_N(2s)$ and $e_{Al}(2p)$ notations stand for the positron annihilations with electrons on 2p, 4d (or 5s), 2p, 2s and 2p orbitals of C, In, O, N and Al, respectively (e); The optimized structure of ICN which is depicted using the ball-and-stick model, with small brown, gray, red, and large violet balls representing C, N, O, and In atoms, respectively (f); STEM image of ICN (h); and STEM-EDS images of ICN (k)

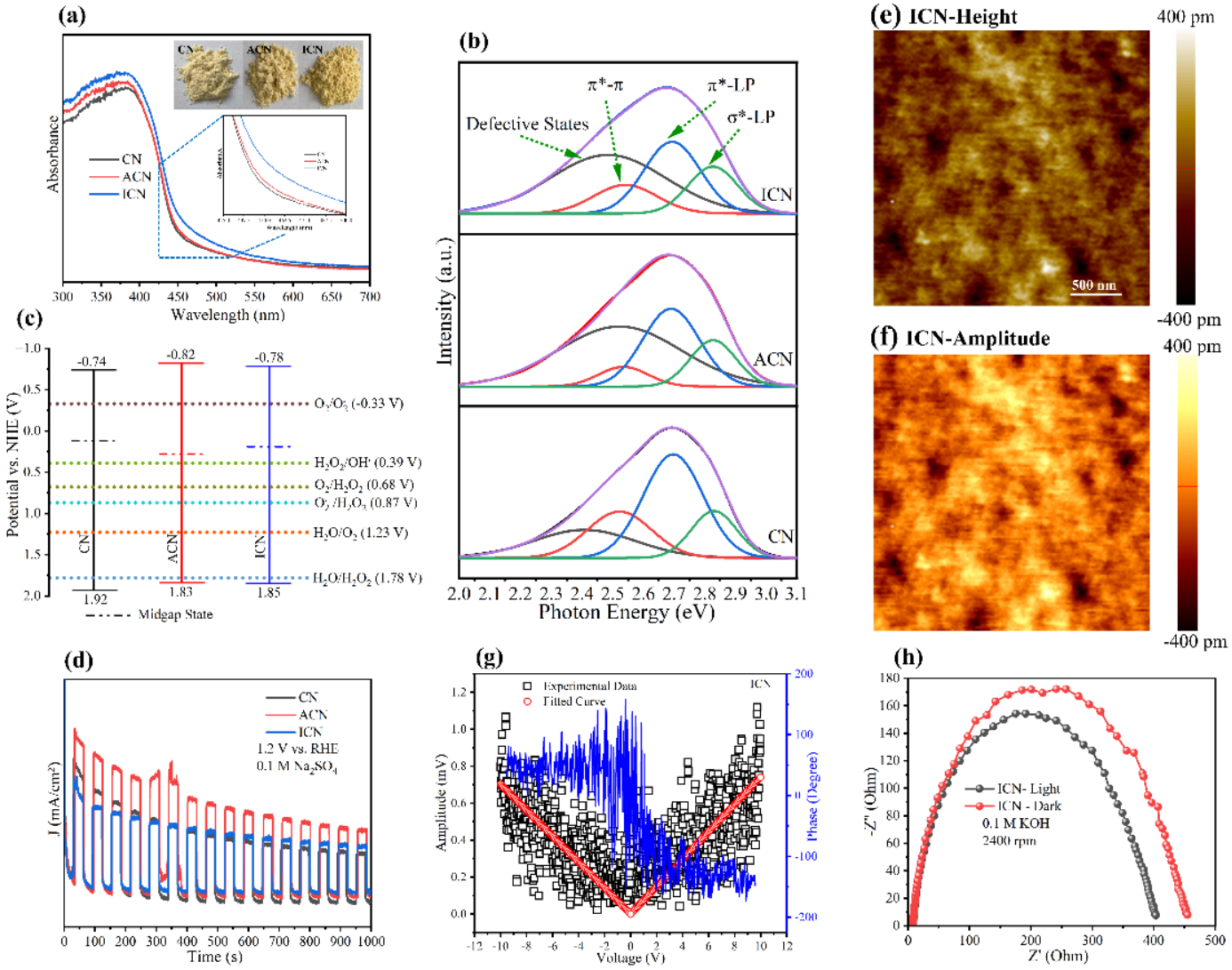

Figure 3

UV-DRS spectra (a); PL energy spectra (b); Band structure diagram (c); Transition photocurrent spectra (d); Piezo-response force microscopy (PFM) images of ICN: height image (e); amplitute image (f); butterfly loop (g); and Piezo-photo EIS results of ICN under light irradiation and darkness (h)

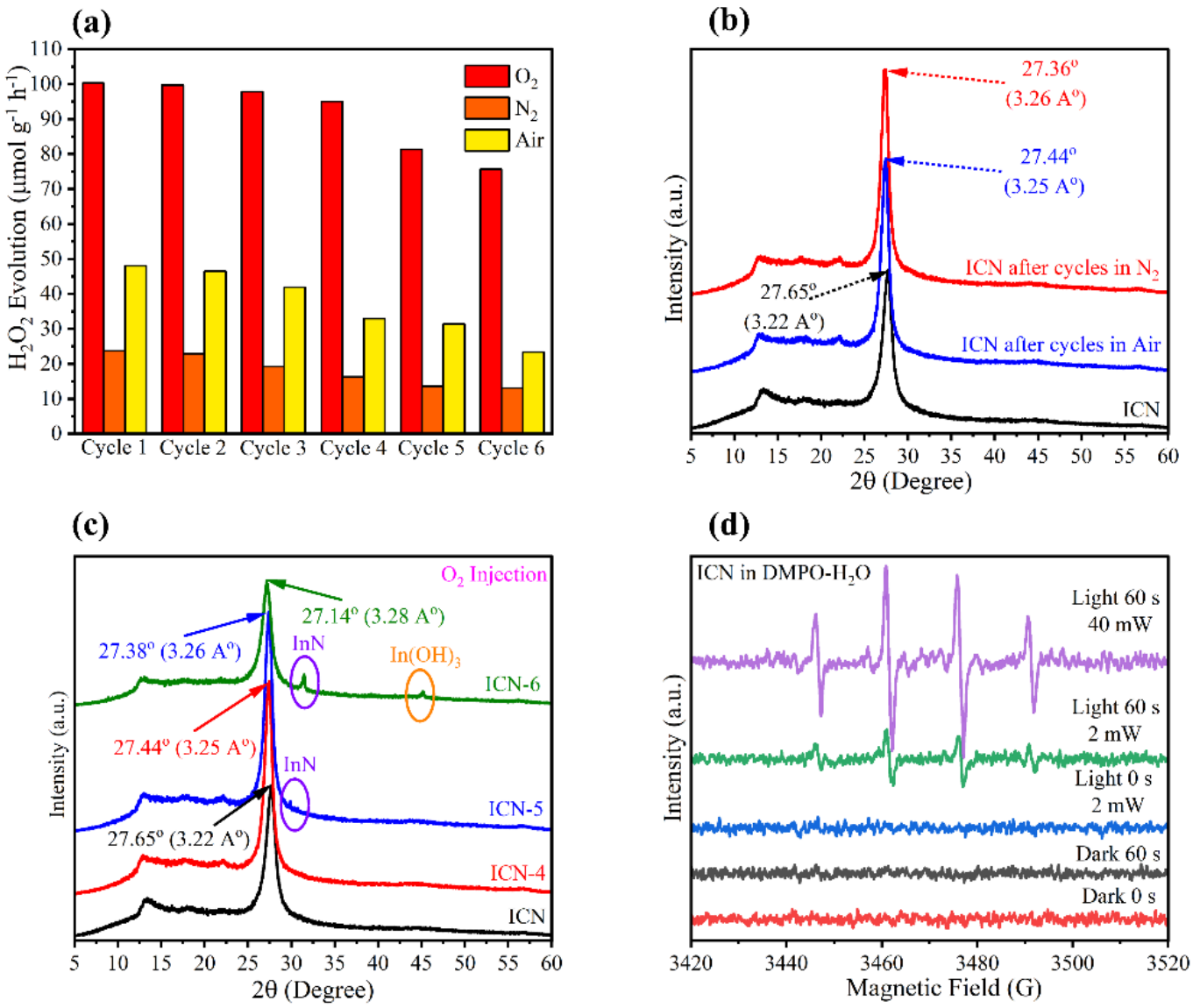

Figure 4

Stability examinations of ICN (200 mf) under different saturated atmospheres (a); XRD patterns of ICN after six cycles under air and N_2 (b); XRD patterns of ICN after four, five, and six cycles under O_2 (c); and In-situ EPR spectra of ICN under dark and light irradiation for hydrogen radical trappings

Supplementary Files

This is a list of supplementary files associated with this preprint. Click to download.

- SupportingInformation.docx